# Intracellular and *in Vivo* Cyanide Mapping via Surface Plasmon Spectroscopy of Single Au−Ag Nanoboxes

Peiyuan Wang,[†,∥] Yujie Bai,[‡,∥] Chi Yao,[†] Xiaomin Li,[†] Lei Zhou,[†] Wenxing Wang,[†] Ahmed Mohamed El-Toni,[§,¶] Jian Zi,[‡,⊥] Dongyuan Zhao,[†] Lei Shi,*[,‡,⊥] and Fan Zhang*[,†]

[†]Department of Chemistry, Collaborative Innovation Center of Chemistry for Energy Materials, State Key Laboratory of Molecular Engineering of Polymers, Fudan University, Shanghai 200433, P. R. China

[‡]Department of Physics, Key Laboratory of Micro and Nano Photonic Structures (MOE) and Key Laboratory of Surface Physics, Fudan University, Shanghai 200433, P. R. China

[§]King Abdullah Institute for Nanotechnology, King Saud University, Riyadh 11451, Saudi Arabia

[¶]Central Metallurgical Research and Development Institute, CMRDI, Helwan, Cairo 11421, Egypt

[⊥]Collaborative Innovation Center of Advanced Microstructures, Fudan University, Shanghai 200433, P. R. China

Ⓢ *Supporting Information*

ABSTRACT: Cyanide is extremely toxic to organisms but difficult to detect in living biological specimens. Here, we report a new CN^- sensing platform based on unmodified Au−Ag alloy nanoboxes that etch in the presence of this analyte, yielding a shift in plasmon frequency that correlates with the analyte concentration. Significantly, when combined with dark field microscopy, these particle probes can be used to measure CN^- concentrations in HeLa cells and *in vivo* in Zebra fish embryos. The limit of detection (LOD) of the novel method is 1 nM (below the acceptable limit defined by the World Health Organization), and finite-difference time-domain (FDTD) calculations are used to understand the CN^--induced spectral shifts.
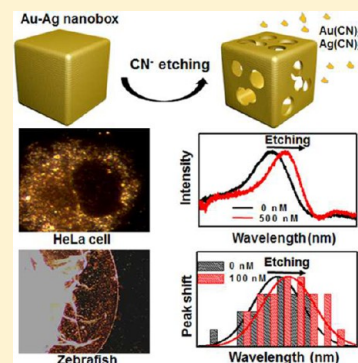
From the standpoint of the environment, cyanide is acutely toxic and can have adverse health effects on biosystems, especially mammals, through many routes of administration.[1,2] On the other hand, cyanide plays crucial roles in many chemical processes, such as petrochemical production, gold mining, metal electroplating, photography, and steel manufacturing.[3] Indeed, approximately one million tons of cyanide products are produced annually for commercial use.[4,5] Additionally, in certain plants and foods, such as cassava roots, fruits, and bitter almonds, cyanide is naturally present.[6,7] Cyanide causes inactivation of cytochrome oxidase (COX), inhibition of cellular respiration, and consequently cellular anoxia.[5,8,9] Furthermore, the uptake of cyanide also increases the level of reactive oxygen species (ROS) and blocks the mitochondrial electron transport chain, which is essential for the synthesis of adenosine triphosphate (ATP).[9] Cyanide can also cause rapid poisoning and adversely affect the central nervous system and heart.[10,11] Titration, spectrophotometry, potentiometry, amperometry, chromatography, and mass spectrometry are currently used to detect cyanide in processed samples, such as blood serum, cell lysates, and homogenized tissues.[12−15] However, none of these methods can be applied to monitor cyanide invasion *in vivo*. Although fluorescent organic molecules and certain nanocomposites have been used to detect cyanide in water, food samples, and even living cells,[16−20] the limit of detection (LOD) of these methods range from 10 to 20 μM[19,21,22] and are much higher than the 1.9 μM acceptable limit set by the World Health Organization.[12] In view of the limitations of the currently available cyanide detection techniques, a sensitive and rapid point-of-care *in vitro* and *in vivo* diagnostic method is needed to detect cyanide and guide the administration of antidotes.

Plasmonic nanocrystals (PNCs) have received significant attention as chemical and biological sensing components due to their local environment-dependent optical properties.[23−28] Importantly, excitation of the localized surface plasmon resonance (LSPR) of PNCs results in wavelength-selective absorption with extremely high molar extinction coefficients ($\sim 3 \times 10^{11}$ M^{-1} cm^{-1}),[29] and resonance Rayleigh scattering has been observed with efficiencies equivalent to that of 10^6 fluorophores,[30] making individual PNCs themselves and corresponding spectral changes readily observable with dark-field microscopy (DFM).[31−35] For biosensing, PNCs act as transducers that convert small changes in the local refractive index into spectral shifts in the intense nanoparticle extinction and scattering spectra through molecular binding.[36] However,
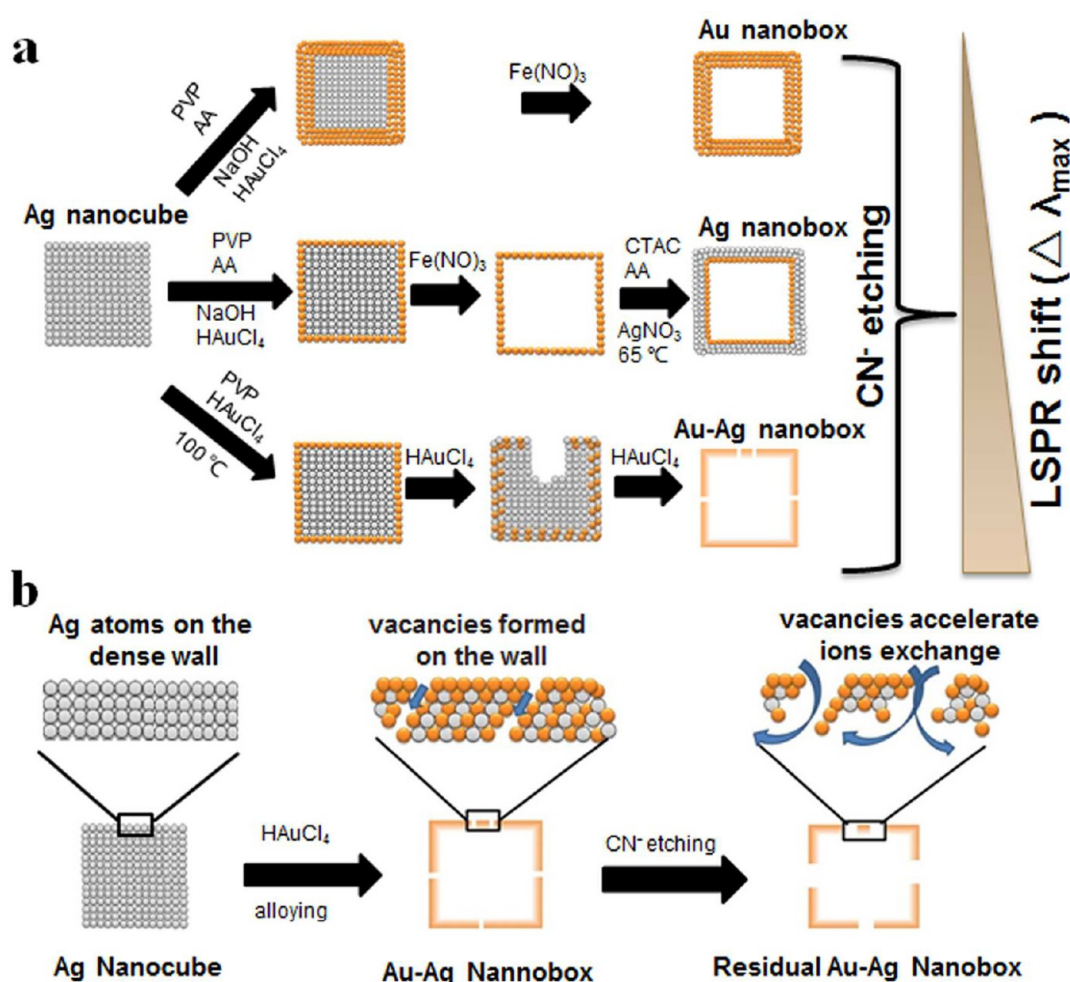
Figure 1. (a) Schematic procedure for the synthesis of Au, Ag, and Au−Ag nanoboxes and the extent of the LSPR shifts ($\Delta\lambda_{max}$) of these nanoboxes after cyanide etching. (b) Schematic illustration of the cyanide etching process. The vacancies of the Au−Ag nanoboxes will accelerate ion exchange during the cyanidation process and enhance the etching effect.

bare nanoparticle surfaces offer limited possibilities for isolating analytes from complex mixtures, especially for *in situ* biosensing. To overcome these limitations, elaborate surface modification strategies often are used to improve sensitivity and selectivity.[36,37] One strategy is to develop PNCs that react with the target in such a way as to modify the particle's composition, size, shape, or orientation, which are strongly correlated with extinction and scattering spectra, instead of passively sensing the tiny local refractive index changes.[29−31]

Herein, we report a new strategy that utilizes a hollow nanostructure made of an Au−Ag alloy that is sensitive to CN⁻. When the nanostructure is exposed to CN⁻, it is etched, which results in a significant change in the LSPR frequency. This can be both a selective and sensitive (LOD = 1 nM) way of measuring CN⁻. Finite-difference time-domain (FDTD) calculations support this conclusion and are consistent with all experimental observations. Finally, we show that variations in local cyanide concentration within HeLa cells and zebrafish embryos can be detected and quantified with nM sensitivity. Taken together, these data show that the individual Au−Ag nanobox approach is ultrasensitive and has the potential to become a powerful new tool for the *in vitro* and *in vivo* mapping of anthropogenic and biogenic cyanide infections.

EXPERIMENTAL SECTION

Synthesis of Au, Ag, and Au−Ag Nanoboxes and Au−Ag Alloys with Different LSPR. Au, Ag, and Au−Ag nanoboxes were synthesized as shown in the schematic procedure and detailed description in the Supporting Information. In order to obtain pure Au nanoboxes, Ag@Au nanocubes were first prepared by directly depositing Au atoms on the surfaces of Ag nanocubes with strong reducing agent ascorbic acid (AA) to compete with and thereby block the galvanic reaction.[38] Then, the inside of Ag nanocubes were eroded with $Fe(NO_3)_3$ to obtain the hollow Au nanoboxes. Ag nanoboxes were synthesized by direct epitaxial deposit of Ag atoms on the surfaces of the Au nanoboxes obtained above.[39] Au−Ag alloys with different Ag to Au ratios were obtained with galvanic replacement reaction by controllable addition of $HAuCl_4$ aqueous solution to a boiled suspension of Ag nanocubes.[40] The reaction can be stopped at any time point to obtain the Au−Ag alloys nanoboxes with a desired LSPR peak.

***In Vitro* and *in Vivo* Cyanide Mapping.** For *in vitro* mapping, a group of Au−Ag nanoboxes was used to sense cyanide with different concentrations (0, 10, 40, 100, 200, and 1000 nM). The solutions were dropped on the coverslips, which were cleaned by using an ultrasonic bath with acetone,
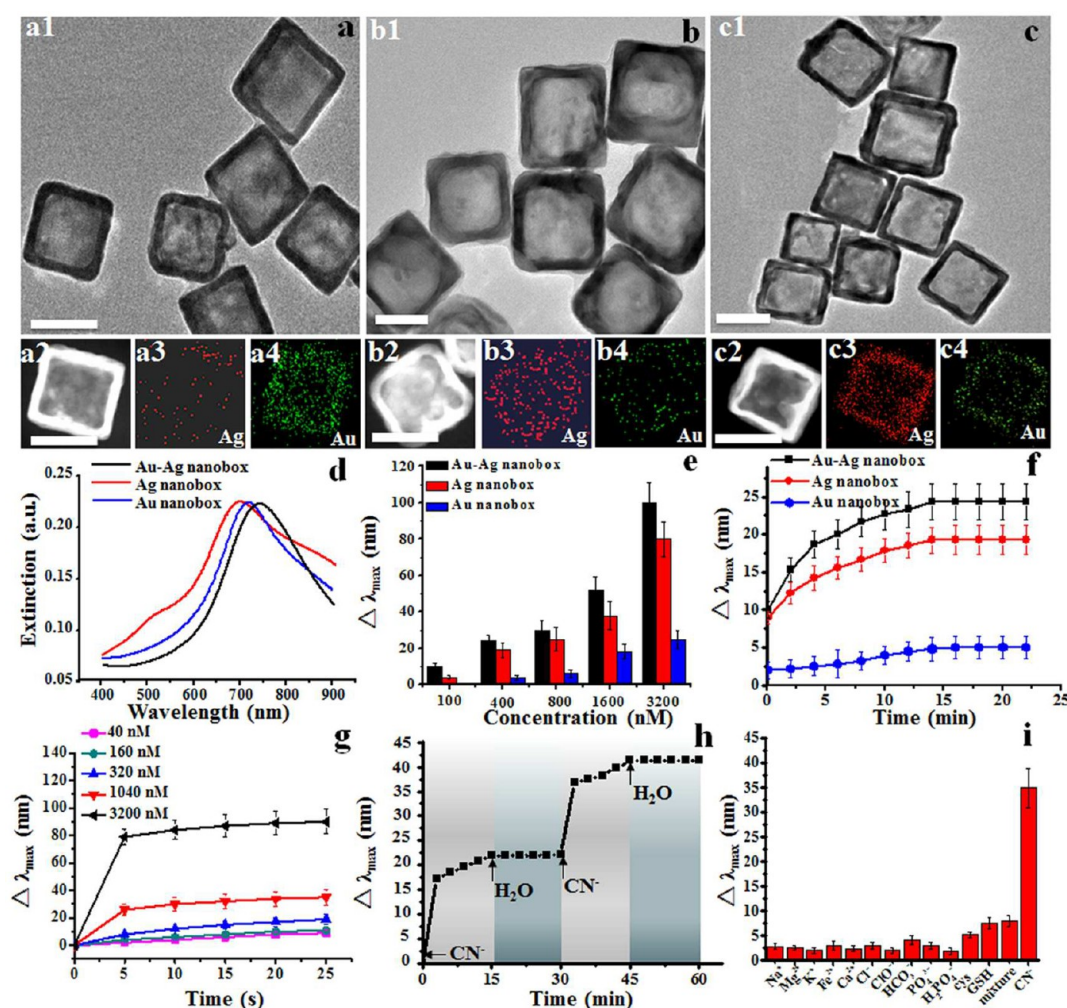
Figure 2. (a−c) TEM, HAADF-STEM, and EDS mapping images of Au, Ag, and Au−Ag nanoboxes. Scale bar represents 50 nm. (d) UV−vis spectra of Au, Ag, and Au−Ag nanoboxes. (e) Equilibrium $\Delta\lambda_{max}$ of cyanide solution after adding 10 nM Au, Ag, and Au−Ag nanoboxes for a 15 min incubation period. (f) Time-dependent $\Delta\lambda_{max}$ with the addition of Au, Ag, and Au−Ag nanoboxes into 400 nM cyanide. (g) Temporal evolution of the $\Delta\lambda_{max}$ of Au−Ag nanoboxes incubated with cyanide solutions for 5−25 s. (h) $\Delta\lambda_{max}$ of Au−Ag nanoboxes after alternately adding 400 nM cyanide and pure water. (i) Selectivity of Au−Ag nanoboxes for intracellular inorganic ions and biothiol. Cysteine (cys) and glutathione (GSH) were 5 mM; other species were 1 μM unless indicated.

methanol, and DI water successively, and then dried by nitrogen. The experiments employed a single particle spectral dark-field microscope with a CCD resolution of 0.6 nm. The *in situ* single particle scattering spectra were also measured by this method. Typically, Au−Ag nanoboxes (10 nM) were dispersed on the coverslip, and then, 5 μL of cyanide (0, 0.5, 1, 5, 10, 100, and 1000 nM) was introduced for 7 min. Finally, after water dried, *in situ* nanoparticle scattering spectra and images were obtained by a single particle spectral dark-field microscope. Time-dependent spectral shifts of single Au−Ag nanoboxes were recorded immediately after adding cyanide of different concentrations (0, 10, 500, 100, and 1000 nM) every 30 s. In order to ensure a complete response, the detection time was as long as 900 s. The *in situ* single Au, Ag, and Au−Ag nanoboxes were dispersed on the coverslip, and then, 100 nM cyanide was introduced, respectively.

For *in vivo* mapping, the cells were cultured on a cleaned cover-glass in a plastic cell culture dish. Internalization of nanoprobes was realized by adding 20 μL (10 nM) of Au−Ag nanoboxes to the cell culture dish and incubating for 4 h. To study cyanide transportation into the cytoplasm and to monitor

intracellular cyanide in real time, the cover-glass was immersed in fresh cell culture medium containing 10, 100, and 500 nM cyanide. Because cell phagocytosis of cyanide was fast, LSPR scattering images and spectra were immediately recorded only after a 7 min incubation. Finally, scattering spectra of two nanoprobes in cytoplasm were recorded *in situ*. The dynamic process of cyanide intracellular endocytosis was observed by incubating Au−Ag nanoboxes with HeLa cells first; time-dependent spectral shifts of single Au−Ag nanoboxes were then measured immediately after 1000 nM cyanide was introduced to HeLa cells.

Zebrafish embryos were collected and transferred into a Petri dish containing nutrient solution (1.2 mM stock salts in deionized (DI) water) and then washed twice with egg water to remove the surrounding debris and placed in 24-well plates with each well containing two embryos in egg water. To study the dose-dependent effects of cyanide on embryonic chorionic space (CS) via chorion pore canals (CPCs), a diluted 741 nm peak Au−Ag nanobox solution (20 nM) was incubated chronically with cleavage-stage (8-cell) embryos in egg water for 12 h. Then, the embryos were transferred to a 100 nM
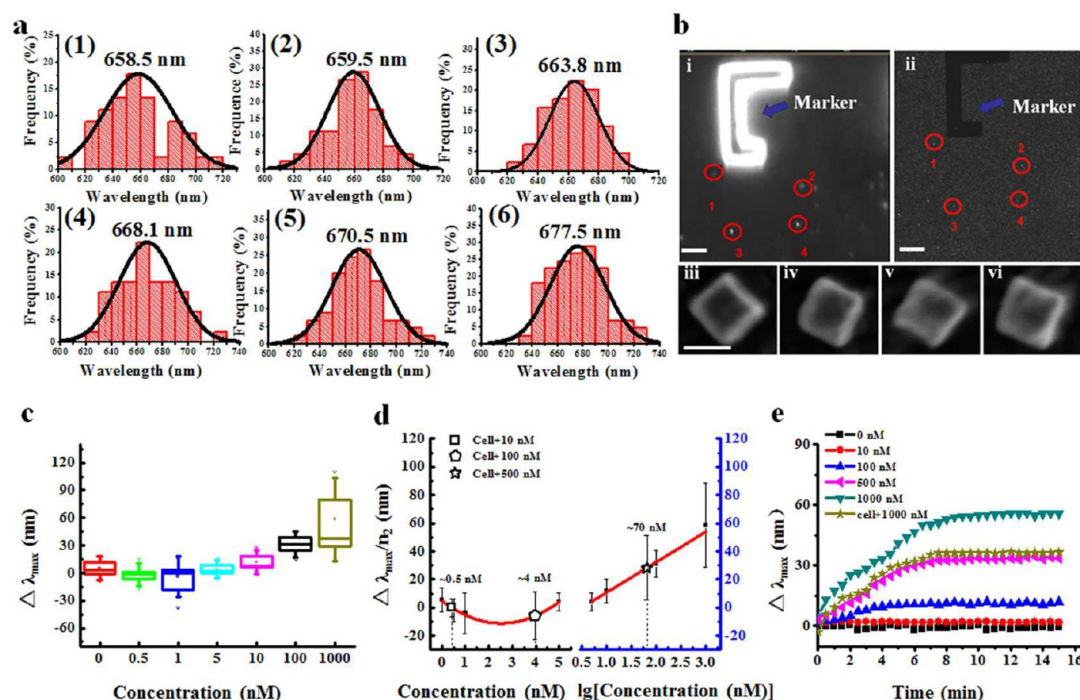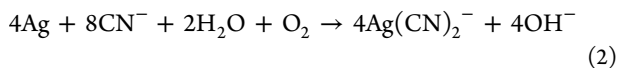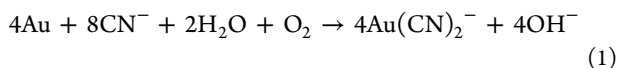
Figure 3. (a) Distribution of LSPR peak wavelengths of Au−Ag nanoboxes after adding 0 (1), 10 (2), 40 (3), 100 (4), 200 (5), and 1000 nM (6) cyanide. More than 60 particles were counted in each case ($N = 60$). (b) Dark-field (i) and SEM (ii−vi) images of Au−Ag nanoboxes fixed on the ITO slide. Red circles were marked to highlight the region of interest. Scale bars represent 10 μm (i, ii) and 50 nm (iii−vi). (c) $\Delta\lambda_{max}$ distribution of 10 single Au−Ag nanoboxes *in situ* treated with cyanide at different concentrations, respectively. (d) Intracellular cyanide detection with a single Au−Ag nanobox. The standard line was collected from (c). HeLa cells were cocultured with 10, 100, and 500 nM cyanide before detection ($N = 10$, error bars = s.d.). (e) Time courses of $\Delta\lambda_{max}$ with cyanide and time-dependent intracellular cyanide sensing with a single Au−Ag nanobox after adding 1000 nM cyanide to the cell culture medium. All spectra were measured at 30 s intervals.

cyanide solution for a 40 min incubation, and the control group was treated with PBS (1×) as the normal condition. The mean values of λ_{max} of cyanide and the normal condition were obtained by using single particle spectral dark-field microscopy.

■ RESULTS AND DISCUSSION

Sensitive Cyanide Sensing in Bulk Solution. Cyanide is able to form very stable complexes, $Au(CN)_2^-$ and $Ag(CN)_2^-$, with Au(0) and Ag(0) at room temperature in the presence of oxygen through strong covalent bonding, a chemical process described as the Elsner reaction.[41]

$$4Au + 8CN^- + 2H_2O + O_2 \rightarrow 4Au(CN)_2^- + 4OH^- \tag{1}$$

$$4Ag + 8CN^- + 2H_2O + O_2 \rightarrow 4Ag(CN)_2^- + 4OH^- \tag{2}$$

Accordingly, it is reasonable to hypothesize that the etching effect of cyanide on Au, Ag, and Au−Ag alloy PNCs will result in a detectable color change or plasmonic extinction spectrum change, leading to the possibility of sensitive cyanide sensing. As shown in the schematic procedure (Figure 1a), a series of PNCs was prepared to study these capabilities for sensing cyanide, including Au and Ag nanocubes and Au, Ag, and Au−Ag nanoboxes (Figures 2a−d and S1−S3). The cubic shape of all the PNCs avoids the curvature effect on the plasmonic extinction spectrum. Figure 2e shows all the equilibrium longitudinal peaks (λ_{max}) of their LSPR spectra shift to longer wavelengths after adding these nanoboxes (10 nM) to different cyanide solutions for 15 min (Figure S4). The Au−Ag nanoboxes with a 741 nm LSPR peak showed the most ideal

sensitivity for cyanide detection both in the temporal phase (5 s) (Figure S5) and at the steady state (15 min). Although Au and Ag nanoboxes also showed attractive sensitivities, the time response of $\Delta\lambda_{max}$ to the addition of these three nanoboxes to 400 nM cyanide solution indicated that, from the initial state to equilibrium, the Au−Ag nanoboxes with the 741 nm LSPR peak respond much more rapidly compared to the Au or Ag nanoboxes (Figures 2f and S6). This sample also showed the best sensitivity for cyanide detection compared to other Au−Ag alloys during galvanic replacement (Figures S7−S9). Furthermore, in comparison to the solid Au and Ag nanocubes (Figure S10), the hollow Au and Ag nanoboxes showed even better sensitivity for cyanide detection, suggesting that the nanobox structure with its hollow cavity and higher specific surface area is also an attractive feature to achieve good detection capability. Because of their superior sensitivity and rapid cyanide sensing ability, attention was paid to the Au−Ag nanoboxes with the 741 nm LSPR peak for cyanide detection. The peak wavelength ($\Delta\lambda_{max}$) of the Au−Ag nanoboxes changed linearly with increasing cyanide concentration (Figure S11a,b). The response time of $\Delta\lambda_{max}$ after adding Au−Ag nanoboxes to a cyanide solution indicated that the Au−Ag nanoboxes responded in 5 s (Figure S11c). When the cyanide concentration changed by as much as 80 times, the temporal time-dependent $\Delta\lambda_{max}$ (5−25 s, Figures 2g and S12) changed by less than 6 times. Interestingly, $\Delta\lambda_{max}$ of Au−Ag nanoboxes showed high sensitivity and remarkable linear response to the 40 nM cyanide (Figure S13). Therefore, it can be concluded that sensitivity up to 40 nM and response time down to 5 s can be realized by the LSPR changes in the solution. Furthermore, the temperature-dependent LSPR shift was also studied, which
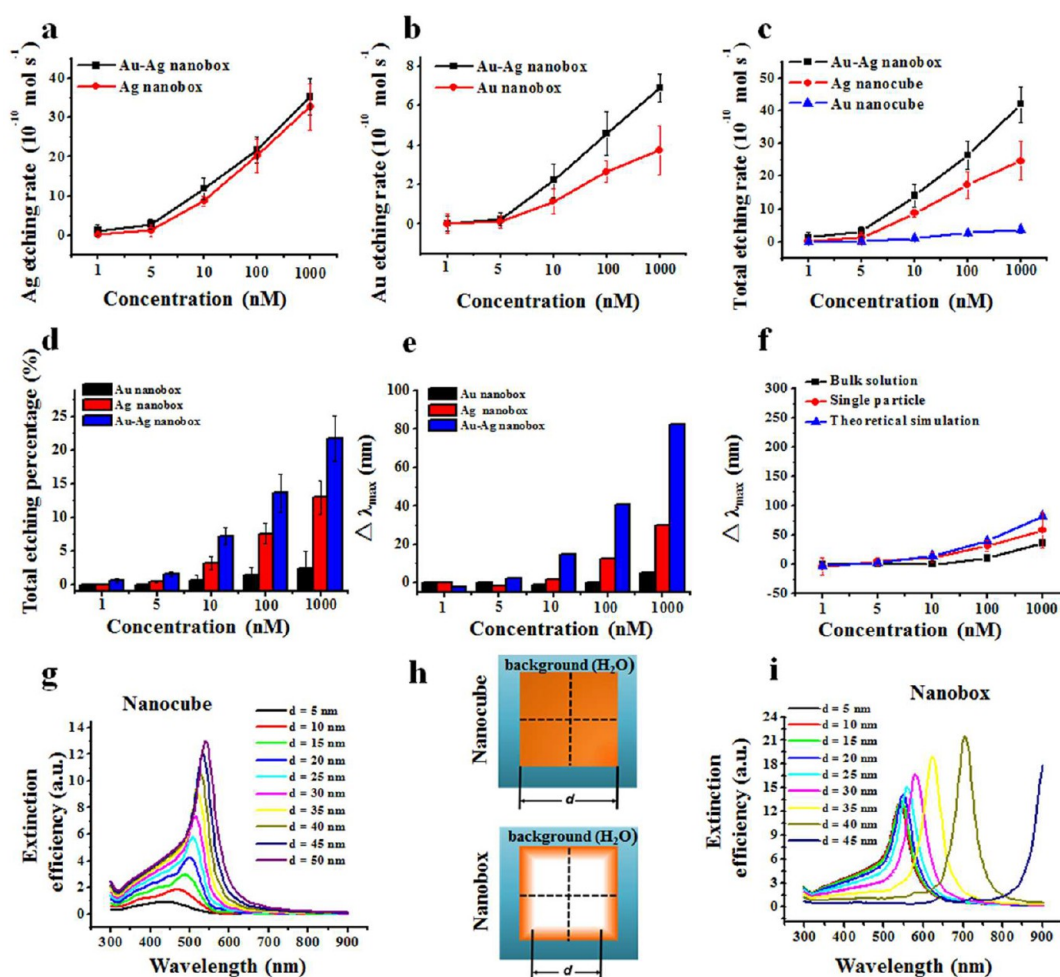
Figure 4. (a) Ag etching rate of Ag and Au−Ag nanoboxes. (b) Au etching rate of Au and Au−Ag nanoboxes. (c) Total etching rate of Au, Ag, and Au−Ag nanoboxes. Total etching percentage (d) and theoretical (FDTD simulations) LSPR spectrum shifts ($\Delta\lambda_{max}$) (e) of Au, Ag, and Au−Ag nanoboxes were obtained after etching at different cyanide concentrations. (f) Comparison of $\Delta\lambda_{max}$ values of Au−Ag nanoboxes between theoretical simulations, single-particle, and bulk solution sensing for cyanide detection. (g) FDTD simulated extinction efficiency of Au−Ag nanocubes with different edge lengths. (h) Illustrations of a nanocube and nanobox during simulations, corresponding to (g) and (i), respectively. (i) FDTD simulated extinction efficiency of Au−Ag alloy nanoboxes with different wall thicknesses.

shows that no significant difference for the LSPR shift can be observed when the temperature was increased from 25 to 50 °C (Figure S14).

An "ON−OFF" effect was observed when cyanide and pure water were alternately added to the Au−Ag nanoboxes fixed in a cuvette, indicating that these nanoprobes were capable of tracking cyanide variations (Figure 2h). Au−Ag nanoboxes showed ideal selectivity toward a mixture of the conventional species, biothiol of cysteine (cys), and glutathione (GSH) found in cells (Zn$^+$, Na$^+$, K$^+$, Mg^{2+}, Fe^{2+}, Ca^{2+}, Cl$^-$, ClO$^-$, HCO$_3^-$, PO$_4^{3-}$, H$_2$PO$_4^-$, 1 μM, cys and GSH, 5 mM) (Figure 2i).

Cyanide Detection via Single-Particle Spectral Imaging. To investigate the potential applications of these individual Au−Ag nanoboxes for cyanide sensing, the plasmon resonance scattering (PRS) spectra of a single particle was used to probe the local cyanide concentration. Because each Au−Ag nanobox is unique in terms of composition and structure, PRS can be identified in a statistical way. After adding Au−Ag nanoboxes to cyanide solutions with different concentrations for 15 min of incubation, the scattering spectra of more than 60 Au−Ag nanoboxes fixed on a microscope slide were measured after the

aqueous solution evaporated. Figure 3a shows the Gaussian distribution of the obtained peak wavelengths λ_{max} of single Au−Ag nanoboxes before and after adding cyanide. A distinct peak shift toward longer wavelengths could be observed in the presence of cyanide. After treatment with 1000 nM cyanide, the most probable λ_{max} was observed with an obvious shift from 658.5 to 677.5 nm. Even an ∼1 nm shift of λ_{max} was observed when the single nanoprobe was treated by a cyanide solution of just 10 nM.

To investigate the *in situ* sensitivity of individual nanoparticles, the single-nanobox probes were fixed on a glass substrate and then immersed in cyanide solutions with different concentrations. The scattering spectrum from each nanobox was measured before and after the immersion. To guarantee the spectra obtained were indeed from the isolated single nanobox, all measured nanoboxes were individually checked using the SEM image (Figure 3b). When the cyanide concentration was below 1 nM, a remarkable wavelength blueshift (2 nm) was observed. The redshift of λ_{max} was observed for cyanide concentrations more than 5 nM (Figure 3c). These results coincided well with the statistical λ_{max} distributions (Figure 3a) and obviously showed the sensitive LOD (1 nM) of this
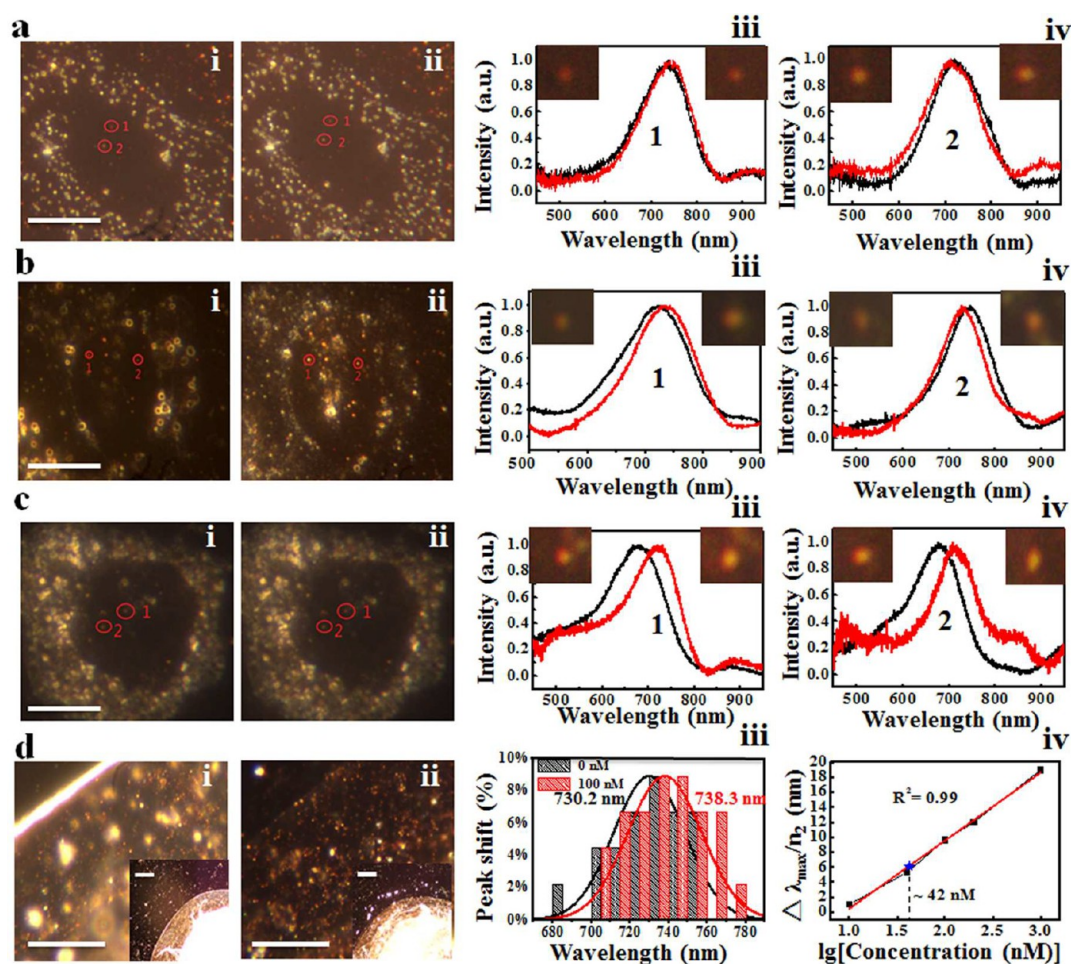
Figure 5. (a−c) DFM images and $\Delta\lambda_{max}$ changes of the dispersed Au−Ag nanoboxes in cytoplasm before (ai, bi, and ci: black line in aiii, biii, and ciii) and after (aii, bii, and cii: red line in aiv, biv, and civ) 10 (a), 100 (b), and 500 nM (c) cyanide treatment. Scale bar, 10 μm. (d) DFM images of an individual zebrafish embryo (di and dii: scale bar represents 15 μm; inset shows the large scale images, with scale bar of 20 μm) before (di) and after 100 nM cyanide treatment (dii). (diii) $\Delta\lambda_{max}$ distributions of Au−Ag nanoboxes under normal conditions (black line) and after 100 nM cyanide (red line) treatment. (div) Inner-embryo cyanide concentration detected by a single Au−Ag nanobox under 100 nM cyanide incubation (blue star). The concentration of cyanide on the standard line was calculated on a log scale based on the center of the λ_{max} distribution in Figure 3a.

method. Because each nanobox acted as an independent cyanide probe, the local amount of cyanide on the nanoscale could be monitored, and the effective "detection volume" of every nanoprobe was thus increased, making it possible to accumulate or react with more cyanide locally to achieve a low detection limit. Furthermore, time-dependent spectral shifts of single Au−Ag nanoboxes were also measured when treated with cyanide (Figure 3e). The experimental results showed that, in all cases, $\Delta\lambda_{max}$ initially increased rapidly but then slowed down. With such a dynamic result, local cyanide concentrations were determined in real time by using the time-dependent results of individual nanoparticles for different fixed cyanide concentrations as external calibration curves for the dynamic process of cellular endocytosis of cyanide.

Mechanism and Theoretical Simulation for Cyanide Sensing. The LSPR spectrum shift decrease should be attributed to the etching effect of cyanide on the Au−Ag nanoboxes, which eventually affects their plasmonic spectra directly (Figure S15). This etching evidence inspired us to measure the removal rate of gold and silver of different PNCs to reveal the underlying mechanism. Compared with other Au−Ag alloys (with LSPR peaks at 538, 680, 741, 826, and 863 nm), the Au−Ag nanoboxes with the 741 nm LSPR showed the

highest etching rate by inductively coupled plasma mass spectrometry (ICPMS) analysis, further demonstrating their superior sensitivity (Figure S16). The galvanic replacement reaction could be separated into three stages: (i) formation of Au−Ag alloyed nanoboxes; (ii) dealloying of the Au−Ag nanoboxes; (iii) fragmentation of the nanoboxes into discrete nanostructures. Compared with alloys with LSPR < 741 nm, this highest etching rate is mainly attributed to the smooth and seamless surface of the hollow nanobox structure and higher specific surface area.[8,40] Compared with alloys with LSPR > 741 nm, in which the pure silver leaching rate in cyanide solution was significantly faster than that of gold,[42] Au−Ag nanoboxes contained higher amounts of silver which can be an ideal nanomaterial for cyanide detection. Furthermore, the removal rate of gold and silver from the Au−Ag nanoboxes was higher than that from either pure Au nanoboxes or pure Ag nanoboxes (Figure 4a,b). Ag nanoboxes were etched significantly faster than Au nanoboxes because of pure Au being less surface passive, similar to bulk Au compared to bulk Ag materials.[42] Furthermore, the faster etching result of Au−Ag nanoboxes is different from that of Au nanoboxes due to the enhancing effect of Ag on Au dissolution.[42] However, the fact that Au−Ag nanoboxes were etched even more quickly than Ag nanoboxes

is a very interesting phenomenon (Figure 4c, etching rate of nanoboxes: Au–Ag > Ag > Au); compared with pure Ag nanoboxes, the silver percentage of the Au–Ag nanoboxes was considerably lower after the cyanide etching (Figure S17), which is different from the bulk materials (etching rate of bulk metals: Ag > Au–Ag > Au).[42] This might be due to the different formation mechanisms of Au–Ag alloy nanoboxes and Ag nanoboxes. Because of their higher redox activity, during Ag nanobox formation, the Ag atoms deposit on the Au nanoboxes layer by layer to form a uniform coating.[43] However, the galvanic replacement reaction to form Au–Ag nanoboxes was initiated via a mechanism involving vacancies formed through the removal of Ag atoms to the outmost layer during the deposition of Au.[44] Therefore, the vacancies of the Au–Ag nanoboxes will accelerate ion exchange during the cyanidation process and enhance the etching effect (Figures 1b and S18).

To understand the dependence of the LSPR on the etching process in detail, FDTD simulations were used to model the scattering of light by a nanobox for different etching stages. The optical properties of metal nanomaterials are determined by a set of parameters that include composition, particle size and shape, overall architecture, and local environment. Interestingly, the residual sliver percentage was less than that of gold (Figure S19a), which indicates that the residual ratio of Ag to Au declined with a cyanide concentration increase (Figure S19b). Moreover, the composition-dependent dielectric index of Au–Ag nanoboxes was calculated by $\varepsilon_{\text{Au–Ag nanoboxes}} = x \times \varepsilon_{\text{Au}} + y \times \varepsilon_{\text{Ag}}$ (x = residual silver percentage, y = residual gold percentage) (Figure S20). The calculated results of the LSPR shift (Figures 4e and S21) are based on the dielectric index and total etching percentage values (characterized by ICPMS in the presence of different amounts of cyanide) of Au, Ag, and Au–Ag nanoboxes (Figure 4d). Obviously, because the sensitivity of the Au–Ag nanoboxes is much higher than that of the Au and Ag nanoboxes (Figures 4e and S21), an LSPR spectrum redshift ($\Delta\lambda_{\text{max}}$) as large as 2.1 nm was observed for Au–Ag nanoboxes when the cyanide concentration was above 5 nM. In contrast, with cyanide concentrations as low as 1 nM, a 2.0 nm blueshift of the LSPR ($\Delta\lambda_{\text{max}}$) was observed. This complex behavior of the resonant wavelength of the nanobox as a function of the cyanide concentration is due to competitive contributions from the volume and wall thickness of the nanoboxes. For a nanocube, only the volume is reduced by cyanide etching, resulting in a blueshift of the plasmon resonance peak[45] (Figure 4g,h). For a nanobox, not only the volume but also the effective wall thickness was reduced by the etching effect (Figure 4h,i). The coupling strength between the inner and outer surface of a nanobox depends on the wall thickness of a core–shell plasmonic structure, and the decrease in the wall thickness will result in a distinct redshift of the plasmonic resonance peak. During the etching process, the cyanide molecules tend to etch the edge and the corners of the nanobox initially in the low concentration stage (∼1 nM), and only the effective volume of the Au–Ag nanoparticle was reduced, resulting in a blueshift. With increasing cyanide concentration (≥5 nM), holes appeared in the nanobox wall and dramatically reduced the effective wall thickness, which will induce a redshift of the LSPR peak as a result of the thickness effect. These simulation results of the Au–Ag nanoboxes are consistent with cyanide sensing behavior for the experimental results of the bulk solution and single nanoparticle sensing (Figure 4f).

Real-Time Cyanide Mapping in Live HeLa Cells and Zebra Fish Embryos. Au–Ag nanoboxes can penetrate the

cell membrane into the cell interior and disperse around the nucleus and lysosomes after coincubation, where the Au–Ag nanoboxes appeared as bright red spots under dark-field illumination (Figure 5ai–ci). *In situ* concentration-dependent spectra of typically two Au–Ag nanoboxes in a single HeLa cell were recorded simultaneously for different cyanide concentrations (Figure 5aii–cii). Figure 5aiii,aiv shows no spectral shift for these two particles. Because of the difference in refractive index of air ($n_1 = 1$, *in situ* single particle detection in Figure 3c) and cytolymph ($n_2 = 1.33$), the intracellular cyanide concentration was finally estimated by $\Delta\lambda_{\text{max}}/n_2$ in Figure 3d. The calibration line on the left side of Figure 3d shows a noticeable blueshift up to 0.5 nM and later reached a maximum at 2.5 nM. In addition, the LSPR blueshift decreased with increasing cyanide up to 5 nM; then, a redshift can be detected. The LSPR redshift on the right side of Figure 3d exhibits a good standard calibration curve on a log scale. According to the *in vitro* calibration result, the local intracellular cyanide concentration was ∼0.5 nM after 10 nM cyanide was introduced. The scattering spectra after introducing 100 nM cyanide (Figure 5b) showed both redshift and blueshift behaviors, and the intracellular local cyanide concentration can be evaluated to be ∼4 nM (Figure 3d). Only a redshift of the LSPR peak was detected in the HeLa cell when 500 nM cyanide was introduced (Figure 5c). The intracellular cyanide concentration was estimated to be ∼70 nM (Figure 3d). The cyanide concentrations inside the cell for each group were 0.5, 5, and 85 nM, respectively, according to a standard spectrophotometry measurement (Figure S22), which is consistent with the DFM results of the single nanobox detection. Furthermore, the dynamic process of intracellular endocytosis by cyanide was also tracked by the Au–Ag nanoboxes (Figure 3e). After the cells were incubated with Au–Ag nanoboxes, the response time of $\Delta\lambda_{\text{max}}$ can be successfully obtained, resulting from intracellular cyanide endocytosis. When 1000 nM cyanide was added, there was a blueshift in 5 s, indicating the cyanide concentration inside the cell was ∼1 nM. A redshift of λ_{max} was observed later, and the calculated intracellular cyanide concentration rose quickly to ∼100 nM in 30 s. The $\Delta\lambda_{\text{max}}$ first increased rapidly to the plateau value in 7 min, and a final intracellular cyanide concentration of ∼500 nM can be detected (Figure 3d). Although each measured cyanide concentration might deviate more or less from the true value due to some systematic errors, such as the unique composition and structure of each PNC, the magnitudes as well as the trends of the results are nevertheless reliable.

The transparent zebrafish embryo is an ideal animal model to monitor the *in vivo* analysis capability of PNCs because of the convenient detection of the LSPR signal by DFM and the ideal permeability of ions and sensors in its body. To evaluate the cyanide concentration in a zebrafish embryo, the λ_{max} distributions of 30 selected nanoprobes captured in zebrafish embryos under normal conditions (0 nM cyanide) (Figure 5di) and 100 nM cyanide incubation conditions (Figure 5dii) were obtained by DFM. Figure 5diii shows the λ_{max} distributions of Au–Ag nanoboxes dispersed in chorion pore canals of a single living embryo under cyanide incubation and normal conditions, respectively. Compared with the normal sample, the mean value of $\Delta\lambda_{\text{max}}$ was ∼8 nm after incubating with 100 nM cyanide. The concentration of cyanide on the standard line was calculated on a log scale based on the center of the λ_{max} distribution in Figure 3a. Because of the difference in refractive index between air ($n_1 = 1$, Figure 3a) and water in the zebrafish

chorionic villi (n_2 = 1.33), the inner-embryo cyanide concentration was estimated by $\Delta\lambda_{max}/n_2$ in Figure 5div; the cyanide concentration in the chorionic villi of zebrafish can be estimated to be ∼42 nM. This concentration was comparable to the spectrophotometry result (Figure S22), which also showed that the cyanide concentration in the chorion was approximately 45 nM after incubation with 100 nM cyanide. This rapid detection of local variations of cyanide concentration in HeLa cell and zebrafish embryo models indicated that the Au−Ag nanobox-based sensing system could offer an exciting platform for *in vivo* cyanide detection at the nM level.

Toxic Cell Damage by Cyanide. To demonstrate that the LOD of this *in situ* Au−Ag nanobox system for cyanide detection is lower than the toxic damage margin of cells and reveal its early warning capability for cyanide poisoning of organisms, the instant cytotoxicity of the cyanide on cells was investigated by measuring the cell viability and the activity of cytochrome oxidase (Figures S23−28). On the basis of the cytotoxicity results, it is believed that cyanide with a concentration 200 nM is hazardous to cells. Furthermore, concentrations of cyanide higher than 40 nM are typically associated with acute cytochrome oxidase poisoning. Fortunately, the single-nanobox detection approach with the Au−Ag nanoboxes reported in this work can realize a LOD down to 1 nM for both *in vivo* and *in vitro* detection, which will provide an approach to forecast the cyanide poisoning of living organisms.

CONCLUSION

In summary, a series of PNCs was synthesized, and hollow Au−Ag nanoboxes were demonstrated as an ideal nanosensor comprising a reactive surface structure as well as its plasmonic coupling feature for sensitive cyanide detection. As a technique that essentially measures cyanide at the single particle level, this integrative sensing approach, based on an individual Au−Ag nanobox imaging method, could be utilized to develop sensitive detection of cyanide *in vivo* and *in vitro*. It is believed that the present demonstration will provide a major step toward the early warning of cyanide toxicity of organisms. Furthermore, as a technique that essentially measures localized concentration by a single PNP (Plug-and-Play) imaging method, it could potentially be utilized to develop highly sensitive detection methods for other small molecules or ions based on direct or indirect chemical modifications of PNCs.

ASSOCIATED CONTENT

Ⓢ Supporting Information

The Supporting Information is available free of charge on the ACS Publications website at DOI: 10.1021/acs.anal-chem.6b04860.

> Experimental section; TEM images; extinction spectra; photos of vials containing Ag nanocubes and Au−Ag alloys; UV-vis absorbance spectra; time-dependent extinction spectra; EDX mapping images; $\Delta\lambda_{max}$ and ΔI analyses; SEM images; Au and Ag etching rate; residual silver percentage of Ag and Au−Ag nanoboxes; residual silver/gold molar percentage and residual molar ratio of silver to gold of Au−Ag nanoboxes; material dielectric index in Lumerical material table; theoretical FDTD simulation; calibration plot of the intensity of the Fe^{3+} absorption peak with different cyanide concentrations; cytotoxicity of cyanide towards HeLa cells; confocal images; histogram of cytochrome oxidase

activity; flow cytometry data; Western blotting analysis (PDF)

AUTHOR INFORMATION

Corresponding Authors
*E-mail: zhang_fan@fudan.edu.cn. Tel.: (+86)21-51630322. Fax: (+86)21-5163-0307.
*E-mail: lshi@fudan.edu.cn. Tel.: (+86)21-55664150; Fax: (+86)21-65104949.

ORCID 🄾
Dongyuan Zhao: 0000-0001-8440-6902
Fan Zhang: 0000-0001-7886-6144

Author Contributions
∥P.W. and Y.B. contributed equally.

Notes
The authors declare no competing financial interest.

REFERENCES

(1) Smith, A. D.; Duckett, S.; Waters, A. H. *Nature* **1963**, *200*, 179−181.
(2) Rothman, S. M. *Science* **1983**, *220*, 536−537.
(3) Xu, Z. C.; Chen, X. Q.; Kim, H. N.; Yoon, J. Y. *Chem. Soc. Rev.* **2010**, *39*, 127−137.
(4) Mudder, T.; Botz, M. *Min. Env. Man.* **2001**, *9*, 8−12.
(5) Koening, R. *Science* **2000**, *287*, 1737−1738.
(6) Ros-Lis, J. V.; Martínez-Máñez, R.; Soto, J. *Chem. Commun.* **2005**, *42*, 5260−5262.
(7) Flematti, F. G.; Merritt, J. D.; Piggott, M. J.; Trengove, R. D.; Smith, S. M.; Dixon, K. W.; Ghisalberti, E. L. *Nat. Commun.* **2011**, *2*, 360.
(8) Hudnall, T. W.; Gabbaï, F. P. *J. Am. Chem. Soc.* **2007**, *129*, 11978−11986.
(9) Green, D. R.; Reed, J. C. *Science* **1998**, *281*, 1309−1312.
(10) Nonaka, S.; Hough, C. J.; Chuang, D.-M. *Proc. Natl. Acad. Sci. U. S. A.* **1998**, *95*, 2642−2647.
(11) Gunasekar, P. G.; Sun, P. W.; Kanthasamy, A. G.; Borowitz, J. L.; Isom, G. E. *J. Pharmacol. Exp. Ther.* **1996**, *277*, 150−155.
(12) Shan, D.; Mousty, C.; Cosnier, S. *Anal. Chem.* **2004**, *76*, 178−183.
(13) Ishii, A.; Seno, H.; Watanabe-Suzuki, K.; Suzuki, O.; Kumazawa, T. *Anal. Chem.* **1998**, *70*, 4873−4876.
(14) Suzuki, T.; Hioki, A.; Kurahashi, M. *Anal. Chim. Acta* **2003**, *476*, 159−165.
(15) Safavi, A.; Maleki, N.; Shahbaazi, H. R. *Anal. Chim. Acta* **2004**, *503*, 213−221.
(16) Kim, Y.; Zhao, H. Y.; Gabbaï, F. P. *Angew. Chem., Int. Ed.* **2009**, *48*, 4957−4960.
(17) Badugu, R.; Lakowicz, J. R.; Geddes, C. D. *J. Am. Chem. Soc.* **2005**, *127*, 3635−3641.
(18) Yao, L.; Zhou, J.; Liu, J.; Feng, W.; Li, F. Y. *Adv. Funct. Mater.* **2012**, *22*, 2667−2672.
(19) Liu, J.; Liu, Y.; Liu, Q.; Li, C.; Sun, L.; Li, F. Y. *J. Am. Chem. Soc.* **2011**, *133*, 15276−15279.
(20) Liu, Y.; Ai, K.; Cheng, X.; Huo, L.; Lu, L. *Adv. Funct. Mater.* **2010**, *20*, 951−957.

(21) Anzenbacher, P.; Tyson, D. S.; Jursíková, K.; Castellano, F. N. *J. Am. Chem. Soc.* **2002**, *124*, 6232−6233.

(22) Dai, Z.; Boon, E. M. *J. Am. Chem. Soc.* **2010**, *132*, 11496−11503.

(23) Schreiber, R.; Do, J.; Roller, E.-M.; et al. *Nat. Nanotechnol.* **2014**, *9*, 74−78.

(24) Ross, M. B.; Ku, J. C.; Vaccarezza, V. M.; Schatz, G. C.; Mirkin, C. A. *Nat. Nanotechnol.* **2015**, *10*, 453−458.

(25) Anker, J. N.; Hall, W. P.; Lyandres, O.; Shah, N. C.; Zhao, J.; Van Duyne, R. P. *Nat. Mater.* **2008**, *7*, 442−453.

(26) Yavuz, M. S.; Cheng, Y. Y.; Chen, J. Y.; Cobley, C. M.; Zhang, Q.; Rycenga, M.; Xie, J. W.; Kim, C. H.; Song, K. H.; Schwartz, A. G.; Wang, L. V.; Xia, Y. N. *Nat. Mater.* **2009**, *8*, 935−939.

(27) Chen, H. J.; Shao, L.; Li, Q.; Wang, J. F. *Chem. Soc. Rev.* **2013**, *42*, 2679−2724.

(28) Mubeen, S.; Lee, J.; Singh, N.; Kramer, S.; Stucky, G. D.; Moskovits, M. *Nat. Nanotechnol.* **2013**, *8*, 247−251.

(29) Jensen, T. R.; Malinsky, M. D.; Haynes, C. L.; Van Duyne, R. P. *J. Phys. Chem. B* **2000**, *104*, 10549−10556.

(30) Novo, C.; Funston, A. M.; Pastoriza-Santos, I.; Liz-Marzán, L.; Mulvaney, P. *Angew. Chem., Int. Ed.* **2007**, *46*, 3517−3520.

(31) Jain, P. K.; Huang, X.; El-Sayed, I. H.; El-Sayed, M. A. *Acc. Chem. Res.* **2008**, *41*, 1578−1586.

(32) Alivisatos, P. *Nat. Biotechnol.* **2004**, *22*, 47−52.

(33) Novo, C.; Funston, A. M.; Mulvaney, P. *Nat. Nanotechnol.* **2008**, *3*, 598−602.

(34) Xiong, B.; Zhou, R.; Hao, J.; Jia, Y.; He, Y.; Yeung, E. S. *Nat. Commun.* **2013**, *4*, 1708.

(35) Braun, G. B.; Friman, T.; Pang, H. B.; Pallaoro, A.; Mendoza, T. H.; Willmore, A. A.; Kotamraju, V. R.; Mann, A. P.; She, Z. J.; Sugahara, K. N.; Reich, N. O.; Teesalu, T.; Ruoslahti, E. *Nat. Mater.* **2014**, *13*, 904−911.

(36) Rodriguez-Lorenzo, L.; de la Rica, R.; Alvarez-Puebla, R. A.; Liz-Marzan, L. M.; Stevens, M. M. *Nat. Mater.* **2012**, *11*, 604−607.

(37) Kosaka, P. M.; Pini, V.; Ruz, J. J.; da Silva, R. A.; González, M. U.; Ramos, D.; Calleja, M.; Tamayo, J. *Nat. Nanotechnol.* **2014**, *9*, 1047−1053.

(38) Yang, Y.; Liu, J.; Fu, Z. W.; Qin, D. *J. Am. Chem. Soc.* **2014**, *136*, 8153−8156.

(39) Jing, H.; Zhang, Q.; Large, N.; Yu, C. M.; Blom, D. A.; Nordlander, P.; Wang, H. *Nano Lett.* **2014**, *14*, 3674−3682.

(40) Skrabalak, S. E.; Au, L.; Li, X. D.; Xia, Y. N. *Nat. Protoc.* **2007**, *2*, 2182−2190.

(41) Wang, X.-B.; Wang, Y. L.; Yang, J.; Xing, X. P.; Li, J.; Wang, L. S. *J. Am. Chem. Soc.* **2009**, *131*, 16368−16370.

(42) Dai, X.; Breuer, P. L. *Hydrometallurgy* **2013**, *133*, 139−148.

(43) Sun, Y. G.; Xia, Y. N. *Science* **2002**, *298*, 2176−2179.

(44) Zhang, L.; Roling, L. T.; Wang, X.; Vara, M.; Chi, M.; Liu, J.; Choi, S. I.; Park, J.; Herron, J. A.; Xie, Z.; et al. *Science* **2015**, *349*, 412−416.

(45) Zhang, Q.; Li, W. Y.; Moran, Y.; Zeng, J.; Chen, J. Y.; Wen, L. P.; Xia, Y. N. *J. Am. Chem. Soc.* **2010**, *132*, 11372−11378.